

Fast and Accurate Prediction of Electromagnetic and Temperature Fields for SPMSM Equipped with Unequally Thick Magnetic Poles

Feng Liu, Xiuhe Wang, Lingling Sun, and Hongye Wei

Abstract—With the continuous upgrading of traditional manufacturing industries and the rapid rise of emerging technology fields, the performance requirements for the permanent magnet synchronous motors (PMSMs) have become higher and higher. The importance of fast and accurate electromagnetic thermal coupling analysis of such motors becomes more and more prominent. In view of this, the surface-mounted PMSM (SPMSM) equipped with unequally thick magnetic poles is taken as the main object and its electromagnetic thermal coupling analytical model (ETcAM) is investigated. First, the electromagnetic analytical model (EAM) is studied based on the modified subdomain method. It realizes the fast calculation of key electromagnetic characteristics. Subsequently, the 3D thermal analytical model (TAM) is developed by combining the EAM, the lumped parameter thermal network method (LPTNM), and the partial differential equation of heat flux. It realizes the fast calculation of key thermal characteristics in 3D space. Further, the information transfer channel between EAM and TAM is built with reference to the intrinsic connection between electromagnetic field and temperature field. Thereby, the novel ETcAM is proposed to realize the fast and accurate prediction of electromagnetic and temperature fields. Besides, ETcAM has a lot to commend it. One is that it well accounts for the complex structure, saturation, and heat exchange behavior. Second, it saves a lot of computer resources. It offers boundless possibilities for initial design, scheme evaluation, and optimization of motors. Finally, the validity, accuracy, and practicality of this study are verified by simulation and experiment.

Index Terms—Electromagnetic field and temperature field, Electromagnetic thermal coupling analytical model (ETcAM), Fast and accurate prediction, SPMSM, Unequally thick magnetic poles.

Manuscript received March 24, 2025; revised May 27, 2025; accepted June 16, 2025. Date of publication June 25, 2025; Date of current version June 18, 2025.

This work was supported by the Project of National Natural Science Foundation of China under Grant 52077122.

Feng Liu, and Xiuhe Wang are with the School of Electrical Engineering, Shandong University, Jinan 250061, China (e-mail: liucf1019@mail.sdu.edu.cn; wangxh@sdu.edu.cn).

Lingling Sun is with the School of Mechanical Engineering, Shandong University, Jinan 250061, China (e-mail: sunll@sdu.edu.cn).

Hongye Wei is with the State Grid Shandong Electric Power Company Jinan Power Supply Company, Jinan 250012, China (e-mail: 202114596@mail.sdu.edu.cn).

(Corresponding author: Xiuhe Wang)

Digital Object Identifier 10.30941/CESTEMS.2025.00020

I. INTRODUCTION

A. Research Background

IN the world today, global energy security uncertainty still exists under the influence of many factors, such as climate change, environmental pollution, exchange rate fluctuations, and geopolitical conflicts. In order to fundamentally resolve the energy crisis, it is imperative to accelerate the development of renewable energy and promote the energy transition. In this background, permanent magnet synchronous motors (PMSMs) stand out from the crowd of motors by virtue of outstanding performance [1]-[3]. PMSMs are gradually becoming the main power source and core component in traditional manufacturing industries and emerging technology fields (new energy vehicles, electric ships, aviation aircraft, etc.) [4]-[6]. Therefore, considering that the operational state and performance of PMSMs are directly related to multiphysics fields, such as electromagnetic and temperature fields, the importance of fast and accurate electromagnetic thermal coupling analysis of such motors is becoming increasingly prominent.

B. Research Status

1) Analysis of the Electromagnetic Field

For the analysis of the electromagnetic field of PMSMs, the existing methods have been relatively mature, mainly including the finite element method (FEM) [7], the magnetic equivalent circuit [8], and the precise subdomain method [9]. Among them, along with the revolution of commercial software and computer technology, FEM has been commonly used by virtue of its unique advantages. It can completely consider the influence of the complex structure, material nonlinearity, and other factors, and realize the accurate calculation of key electromagnetic characteristics [10]. However, it still faces a large computational burden and storage pressure, especially when facing the optimization design. On the contrary, the other two methods do not need to occupy much computer resources. Moreover, both of them have received wide attention by virtue of their very good accuracy. However, they also face some challenges. The magnetic equivalent circuit often requires a large number of nodes to support the computational accuracy. This makes the modeling complexity increase dramatically. And, the model generalization is also greatly diminished [11]. The precise

subdomain method requires more effort in the topological equivalence and saturation counting [12].

2) Analysis of the Temperature Field

For the analysis of the temperature field of PMSMs, the existing methods are still limited to the computational fluid dynamics (CFD) [13], the lumped parameter thermal network method (LPTNM) [14], and the analytical method [15]. They all have very obvious advantages and disadvantages. Table I provides a full evaluation of their overall performance. CFD can not be affected by the complex structure, fluid motion state, and material anisotropy, to maximize the restoration of the real heat dissipation environment, simulate the complex heat exchange behavior, and realize the accurate calculation of key thermal characteristics [16]. However, it often needs to face very huge computational burden and storage pressure. Moreover, it has extremely high operational requirements for mesh partitioning and parameter setting. LPTNM does not need to occupy much computer resources. And it can quickly calculate the average temperature of critical components [17]. However, its node construction principle determines that it cannot realize global temperature distribution prediction, let alone hotspot tracking. This limits it to the preliminary design or rough estimation stage, making it difficult to be further applied and developed. In this context, the analytical method has been consistently favored by many scholars for its excellent prediction capability and very low resource consumption [18]. Some temperature prediction models based on the analytical method have been successively developed and applied to conventional PMSMs [19]. The overall performance of these models deserves to be recognized. However, there are some areas that need to be improved urgently. One is that these models are designed to predict the temperature of specific components like permanent magnets (PMs) or windings. As for high-performance PMSMs, excessive operating temperature induces large thermal stress and deformation in addition to the windings short-circuit, the insulation breakage, and the PMs demagnetization. This in turn causes severe mechanical friction, assembly failure, vibration noise, and other harsh consequences. Threatening the safety stability and operational reliability of systems. Therefore, it is one-sided to focus only on the temperature of a particular component. The second is that the prediction dimension of these models is mostly limited to the 2D space. It is not yet possible to realize the prediction of the global temperature for PMSMs in 3D space.

TABLE I
EVALUATION OF DIFFERENT TEMPERATURE FIELD ANALYSIS METHODS

Item	CFD	LPTNM	Analytical method
Time	☹	☹☹☹☹	☹☹☹☹
Storage	☹	☹☹☹☹	☹☹☹☹
Average temp.	☹☹☹☹	☹☹☹☹	☹☹☹☹
Hot spot	☹☹☹☹	☹	☹☹☹☹
2D space temp.	☹☹☹☹	☹	☹☹☹☹
3D space temp.	☹☹☹☹	☹	☹☹☹☹

Note: More “☹” means better performance.

C. Research Motivation

There is a strong coupling between the electromagnetic

field and temperature field of PMSMs. The operating temperatures of PMSMs are different under different load conditions and different heat dissipation environments. Different operating temperatures directly determine the demagnetization curve of PMs and the resistance of windings. This then has an impact on the actual operating state and output performance. Once the electromagnetic characteristics are affected, it will inevitably affect the thermal characteristics in return. The most direct manifestation is to affect the heat dissipation by changing the loss. Hence, it is necessary to perform the electromagnetic thermal coupling analysis for PMSMs instead of the single electromagnetic field or temperature field analysis.

[20] proposed an electromagnetic thermal coupling analytical model based on the analytical method around a permanent magnet synchronous motor. The precise subdomain method and the multiple regression technique are adopted to realize the calculation of key electromagnetic and thermal characteristics, respectively. However, the computational capability of this model is quite limited. Especially in the temperature field calculation, neither the construction of topological network and the solution of node temperature can be accomplished as well as LPTNM, nor the prediction of global temperature distribution can be accomplished as perfectly as analytical method, which is only limited to the calculation of specific reference temperature of a single component. [21] proposed an electromagnetic thermal coupling analytical model (ETcAM) based on the analytical method around a permanent magnet assisted synchronous reluctance motor. The magnetic equivalent circuit and LPTNM are adopted to realize the calculation of key electromagnetic and thermal characteristics, respectively. However, this model is also severely limited by the many shortcomings faced by the previously mentioned existing methods for electromagnetic and temperature field analysis.

This has resulted in the fact that numerical methods (FEM and CFD) are still the most effective and commonly used means of performing electromagnetic thermal coupling analysis. Although having good computational accuracy, they inevitably inherit the inherent defects of FEM and CFD. In particular, this shortcoming will be infinitely magnified when dealing with multiphysics field multiobjective optimization design problems. Therefore, it is very imminent to study the fast and accurate electromagnetic & thermal analytical models as well as to perform the fast and accurate electromagnetic thermal coupling analysis for PMSMs.

D. Research Content

Referring to the previous analysis, this article focuses on the surface-mounted PMSM (SPMSM) equipped with unequally thick magnetic poles, and aims at realizing its fast and accurate prediction of electromagnetic and temperature fields.

1) The electromagnetic analytical model (EAM) is studied based on the modified subdomain method. The irregular structure of unequally thick magnetic poles and saturation are fully accounted for. The fast calculation of key

electromagnetic characteristics is realized.

2) The 3D thermal analytical model (TAM) is developed by combining EAM, LPTNM, and the partial differential equation of heat flux. The irregular structure of unequally thick magnetic poles and the complex heat exchange behavior are fully accounted for. The fast calculation of key thermal characteristics is realized in 3D space.

3) Based on the above study, the information transmission channel between EAM and TAM is built with reference to the intrinsic connection between electromagnetic field and temperature field. The novel ETcAM is proposed. Fast and accurate prediction of electromagnetic and temperature fields is realized. A large amount of computer resources is saved. It offers unlimited possibilities for the initial design, scheme evaluation, and optimization of motors.

Remaining chapters: II, motor topology; III, studied EAM; IV, developed 3D TAM; V, proposed ETcAM; VI, comparison; VII, conclusion; followed by references.

II. MOTOR TOPOLOGY

Fig. 1 depicts the magnetic field modulation behavior of the SPMSM equipped with different magnetic poles. For SPMSM, when equipped with conventional magnetic poles (i.e., PMs with concentric inner and outer diameters), the sinusoidal nature of the air gap magnetic field is poor. The harmonic content is higher. It is easy to further aggravate the degree of cogging torque, torque pulsation, vibration noise, and heat generation. Seriously reduce the energy conversion efficiency. In practical engineering, the sinusoidal nature of the air gap magnetic field is often improved by modifying the shape of the magnetic poles. The unequally thick magnetic poles (i.e., the inner and outer diameters of PMs are not concentric) is one of the most commonly used forms of modification. At the same time, it is widely appreciated because it does not require a cumbersome process or much extra cost. Therefore, the study on the SPMSM equipped with unequally thick magnetic poles is of great scientific value and practical significance.

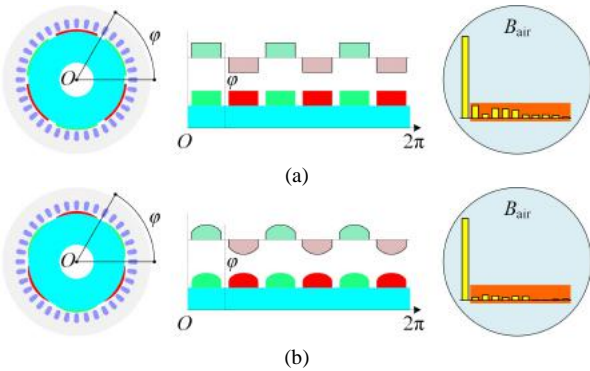


Fig. 1. Magnetic field modulation behavior of SPMSM. (a) Conventional magnetic poles. (b) Unequally thick magnetic poles.

III. ELECTROMAGNETIC ANALYTICAL MODEL

A. Pre-processing of EAM: Topology Equivalence

To facilitate the construction and solving of the EAM, some simple equivalence of the original topology is required.

Fig. 2 depicts the topology before and after the equivalence. The equivalent topology contains four types of subdomains: SD-I, slot; SD-II, slot opening; SD-III, air gap; SD-IV, PM (SD-IV₁, first layer of fan-ring PM; SD-IV₂, second layer of fan-ring PM). It can be seen that SD-I, II, III and IV are featured with periodic annular or sector distribution. Except for SD-IV, all other subdomains can be obtained directly based on the principle of area conservation and constant localization radius. For SD-IV, on the other hand, special handling of unequally thick magnetic poles is required to obtain it. Therefore, in this study, unequally thick magnetic poles are equated to multilayer fan-ring PM.

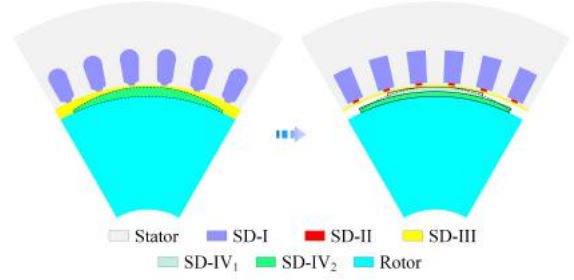


Fig. 2. Topology before and after equivalence.

As depicted in Fig. 3, the unequally thick PM is uniformly subdivided into m layers of fan-ring PM. Where R_1, R_2, \dots, R_m are the outer radii of the first layer fan-ring PM, the second layer fan-ring PM, ..., the m^{th} layer fan-ring PM; $\tau_1, \tau_2, \dots, \tau_m$ are the spanning angles of the first layer fan-ring PM, the second layer fan-ring PM, ..., the m^{th} layer fan-ring PM. According to Pythagorean theorem, the above parameters can be easily obtained by combining the specific number of subdivided layers, the corresponding eccentricity distance, and eccentricity radius at the periphery of the unequally thick PM. It should be declared that, for ensuring clear presentation as well as avoiding redundant elaboration, this study tentatively assumes that the unequally thick PM is subdivided into two layers of fan-ring PM, i.e., m is equal to 2. In practical cases, the number of subdivided layers should be appropriately identified based on the specific topology.

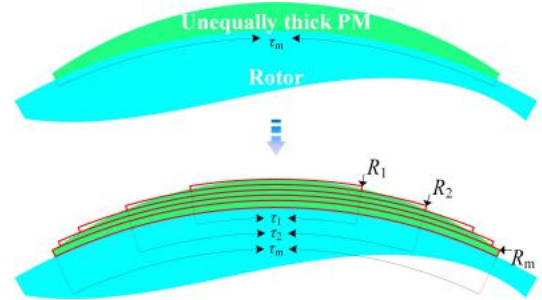


Fig. 3. Equivalence of one unequally thick PM.

B. Construction of EAM: General Solution

The following assumptions are required for the successful construction of EAM:

- 1) Infinite core permeability.
- 2) Linear PM magnetization properties.
- 3) Neglected fringing effects and eddy currents.

It is worth noting that assumption 2) here is not to regard

the PM magnetization property as invariant. Rather, it is adjusted in time in conjunction with the operating temperature during the coupled iterative solution process of ETcAM proposed in the subsequent sections, as shown in Fig. 4. The specific ideas can be summarized in the following four points. First, the reference operating temperature of PM is obtained every time the temperature field is calculated. Subsequently, based on the demagnetization curve at that reference operating temperature, the corresponding linear PM magnetization properties, i.e., remanence and coercive force at that reference operating temperature, are obtained. Further, the electromagnetic field calculation at that reference operating temperature can then be performed. Ultimately, by repeating the above process, the accurate electromagnetic field calculation results are obtained while fully accounting for the deep and strong coupling effect between the electromagnetic field and the temperature field.

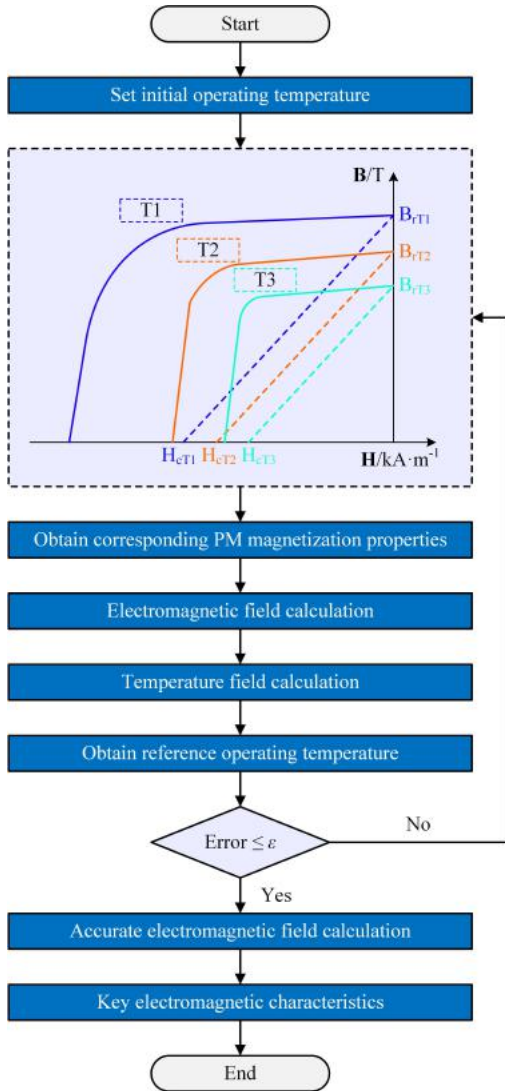


Fig. 4. The determination process of the linear PM magnetization properties.

Based on the relevant assumptions stated previously, the general solution of the vector magnetic potential A_z for each subdomain can be derived. In [22], specific derivation formulas for the general solutions A_z^I , A_z^{II} , and A_z^{III} , for SD-I,

SD-II, and SD-III have been discussed. After that, the general solution A_{zmm}^{IV} of SD-IV $_{mm}$ [the mm^{th} layer fan-ring PM (mm is a positive integer, greater than or equal to 1 and less than or equal to m)] can be expressed as:

$$A_{zmm}^{IV} = \sum_w \left[A_w^{IVmm} \left(\frac{r}{R_{mm}} \right)^w + B_w^{IVmm} \left(\frac{r}{R_{mm-1}} \right)^{-w} \right] \cos(w\alpha) + \sum_w \left[C_w^{IVmm} \left(\frac{r}{R_{mm}} \right)^w + D_w^{IVmm} \left(\frac{r}{R_{mm-1}} \right)^{-w} \right] \sin(w\alpha) + E_{mm} \quad (1)$$

where R_{mm} and R_{mm-1} are the outer and inner radii of SD-IV $_{mm}$, respectively; A_w^{IVmm} , B_w^{IVmm} , C_w^{IVmm} , and D_w^{IVmm} are the coefficients to be solved; E_{mm} is the special solution of A_{zmm}^{IV} ; $w = 1, 2, 3, \dots$

Further, the equivalent surface currents are introduced to approximate the core saturation caused by material nonlinearity [22]. In this way, the negative effect of the assumption of infinite core permeability is well compensated. The prediction accuracy is guaranteed while laying a solid foundation for the smooth construction of EAM. Fig. 5 depicts the face currents in the q^{th} ($q = 1, 2, 3, \dots, Q$, Q is the number of slots) slot of the SD-I. First, taking the q^{th} slot as an example, initial equivalent face currents I_{s1q} and I_{s2q} are added to its left and right sides, respectively. I_{s1q} and I_{s2q} form a loop with the face currents added to the right and left sides of the neighboring slots, respectively. Next, the face currents I_{q1} and I_{q2} on the left and right sides of the q^{th} slot are corrected.

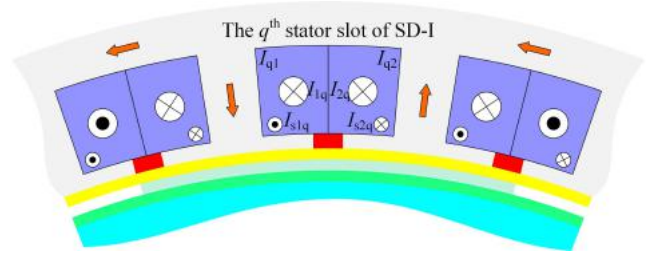


Fig. 5. Face currents in the q^{th} slot of SD-I.

$$\begin{cases} I_{q1} = I_{1q} + I_{s1q} \\ I_{q2} = I_{2q} + I_{s2q} \end{cases} \quad (2)$$

where I_{1q} and I_{2q} denote the currents of the left and right windings in the q^{th} slot, respectively. Then, the vector magnetic potential A_{zq}^I of the q^{th} slot of SD-I is adjusted according to the corrected face currents. Further, the magnetic equivalent circuit and the A_{zq}^I calculated by EAM are combined to obtain new calculation values for the equivalent surface currents. Finally, I_{s1q} and I_{s2q} are adjusted and the above process is repeated using an iterative method until the error is satisfied. In this way, the core saturation caused by material nonlinearity is reasonably approximated in the studied EAM.

C. Solving of EAM

Based on the magnetic field continuity theorem, the

coefficients to be solved contained in the general solution of the vector magnetic potential of each subdomain can be deduced and computed according to the intersection features between neighboring subdomains. This in turn realizes the fast calculation of key electromagnetic characteristics. Thus, the radial air gap flux density B_{r-ag} and the tangential air gap flux density $B_{\alpha-ag}$ can be expressed as:

$$B_{r-ag} = \frac{1}{r} \frac{\partial A_z^{III}}{\partial \alpha} \quad (3)$$

$$B_{\alpha-ag} = -\frac{\partial A_z^{III}}{\partial r} \quad (4)$$

The no-load phase electromotive force can be expressed as:

$$E_{\text{phase}} = -\frac{d\psi}{dt} \quad (5)$$

where ψ is the total flux linkage of each phase.

The electromagnetic torque can be expressed as:

$$T_{\text{em}} = \frac{L_{\text{axial}} R_{\text{ag}}^2}{\mu_0} \int B_{r-ag}(R_{\text{ag}}, \alpha) B_{\alpha-ag}(R_{\text{ag}}, \alpha) d\alpha \quad (6)$$

where L_{axial} is the axial length; R_{ag} is the average radius of the air gap; μ_0 is the vacuum permeability.

The stator core loss can be expressed as:

$$\text{Loss}_{\text{sc}} = \left[c_h f_N B_{\text{core}}^2 + c_e (f_N B_{\text{core}})^{1.5} + c_a (f_N B_{\text{core}})^2 \right] V_{\text{sc}} \quad (7)$$

where c_h , c_e , c_a are hysteresis loss, eddy current loss, and additional loss coefficients, respectively; f_N is the fundamental frequency; B_{core} is the stator core flux density, and V_{sc} is the stator core volume.

IV. 3D THERMAL ANALYTICAL MODEL

Unlike the electromagnetic field, the motor temperature field has a strong three-dimensional character. The heat flow is not only transferred along the radial or circumferential direction in the x - y plane, but also has a significant transfer phenomenon in the z -axis direction, as depicted in Fig. 6.

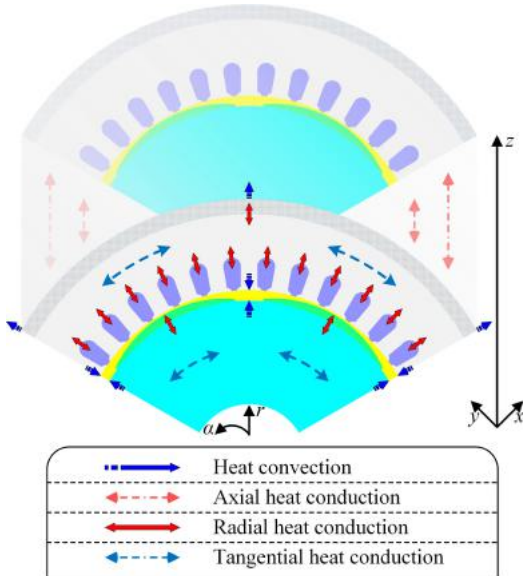


Fig. 6. 3D heat flow distribution.

Therefore, the TAM will be developed starting from the heat exchange behavior in the x - y plane and z -axis direction. As a result, the complex structure and heat exchange behavior of the SPMSM equipped with unequally thick magnetic poles will be fully addressed. The heat dissipation environment will be most realistically reproduced. The fast calculation of key thermal characteristics will be realized.

A. Pre-processing of 3D TAM: Topology Equivalence

To facilitate the construction and solving of the TAM, some simple equivalence of the cross sections of the original topology along the x - y plane and z -axis direction, respectively, is required.

1) x - y Plane

Fig. 7 depicts the topology before and after the equivalent in the x - y plane. The equivalent topology contains nine types of heat zones: HZ-I, housing; HZ-II, stator yoke; HZ-III, stator tooth; HZ-IV, slot; HZ-V, air gap; HZ-VI, side air gap; HZ-VII, interpolar air gap; HZ-VIII, PM (HZ-VIII₁, first layer of fan-ring PM; HZ-VIII₂, second layer of fan-ring PM); HZ-IX, rotor. It can be seen that, similar to the subdomains subdivided in EAM, the heat zones subdivided in the x - y plane by TAM are all featured with periodic annular or sector distribution. Except for HZ-VIII, all other heat zones can be obtained directly based on the principle of area conservation and constant localization radius. For HZ-VIII, special handling of unequally thick magnetic poles is required to obtain it. The specific ones have already been detailed in the relevant parts of EAM.

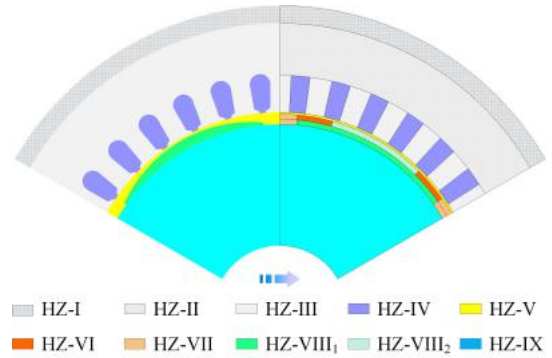


Fig. 7. Equivalent topology in the x - y plane.

2) z -axis Direction

Regarding the topology equivalence in the z -axis direction, the stochastic nature of the cross-section in the z -axis direction varying with angle that needs to be noted. Fig. 8 depicts the four most typical equivalent cross-sections in the z -axis direction. Equivalent cross-section 1 is the cross-section along the z -axis direction at the point where the centerline of the unequally thick PM is aligned with the slot centerline. Equivalent cross-section 2 is a cross-section along the z -axis direction at the point where the centerline of the unequally thick PM is aligned with the tooth centerline. Equivalent cross-section 3 is the cross-section along z -axis direction at the point where the centerline of the interpolar air gap is aligned with the slot centerline. Equivalent cross-section 4 is the cross-section along the z -axis direction at the point where

the centerline of the interpolar air gap is aligned with the tooth centerline. Fig. 9 depicts the distribution of heat zones in the equivalent cross-section 1. There are twelve heat zones containing: HZ-A, housing; HZ-B, stator yoke; HZ-C, slot; HZ-D, air gap; HZ-E, PM; HZ-F, rotor; HZ-G, stator end gap; HZ-H, end winding; HZ-I, winding end gap; HZ-J, rotor end gap; HZ-K, end cap; HZ-L, external air. Similarly, the distribution of equivalent heat zones can be obtained for each cross-section in the z -axis direction varying along the angle. It is only necessary to focus on the variations in the type and size of the heat zones contained in the different cross-sections. For example, the stator tooth in cross-section 2 replaces HZ-C in cross-section 1; the interpolar air gap in cross-section 3 replaces HZ-E in cross-section 1; and the stator tooth in cross-section 4 replaces HZ-C in cross-section 3.

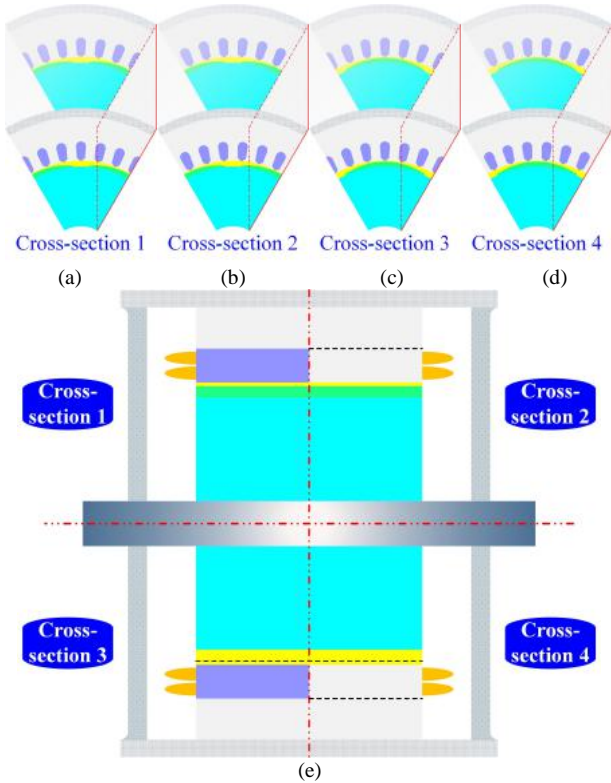


Fig. 8. Typical cross-sections in the z -axis direction. (a) CS 1. (b) CS 2. (c) CS 3. (d) CS 4. (e) All CSs

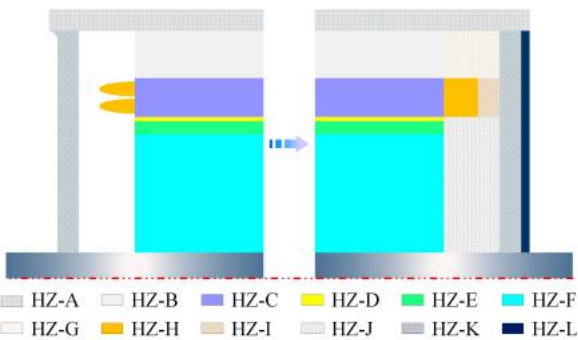


Fig. 9. Equivalent topology in the z -axis direction.

Here, it is worth mentioning that there are many solution cross-sections in the z -axis direction over the entire rotation period. The accurate prediction of the global temperature

distribution, in turn, requires more detailed data support. Therefore, the appropriate solution cross-sections in the z -axis direction should be selected according to the actual engineering needs. As depicted in Fig. 10, a solution cross-section in the z -axis direction can be selected at certain angle intervals along the motor rotation direction. Then, the calculation results on all the solution cross-sections in the z -axis direction are integrated into a single dataset. In this way, it is possible to incorporate the two-dimensional temperature distributions on the different solution cross-sections in different z -axis direction into the solution set of the 3D TAM to obtain a three-dimensional temperature distribution. The specific incorporation method can be performed both by setting a sufficiently large number of solution cross-sections in the z -axis direction and by interpolation techniques. In this article, in order to ensure the solution accuracy of the model and to avoid the estimation error caused by interpolation, one solution cross-section in the z -axis direction is selected at every mechanical angle along the motor rotation direction. In total, 360 solution cross-sections in the z -axis direction are calculated. Finally, the integration of the temperature data on all solution cross-sections in the z -axis direction by means of a simple statistical method provides for the subsequent accurate calculation of the key thermal characteristics.

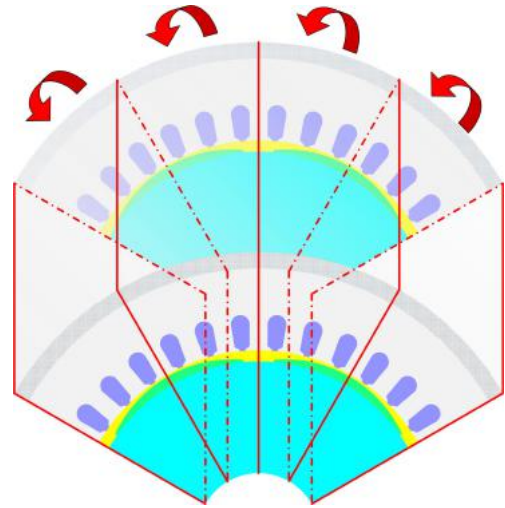


Fig. 10. Solution cross-sections in the z -axis direction.

B. Construction of 3D TAM: General Solution

The following assumptions are required for the successful construction of TAM: 1) neglected assembly clearance; 2) neglected heat radiation. Combined with the partial differential equation of heat flux and the features of nonhomogeneous interfaces, the general solution for the temperature of each heat zone can be derived by applying the superposition principle and the Fourier series expansion.

1) x-y Plane

Based on the actual heat generation during operation, the equivalent heat zones can be divided into two categories: active zones (HZ-II, HZ-III, HZ-IV, HZ-VIII₁, HZ-VIII₂, and HZ-IX) and passive zones (HZ-I, HZ-V, HZ-VI, and HZ-VII). Then, the corresponding heat partial differential equation in the x - y plane can be expressed as:

$$\frac{\partial^2 T}{\partial r^2} + \frac{1}{r} \frac{\partial T}{\partial r} + \frac{1}{r^2} \frac{\partial^2 T}{\partial \alpha^2} = \begin{cases} -P/\lambda & \text{Active zones} \\ 0 & \text{Passive zones} \end{cases} \quad (8)$$

where T is the temperature distribution function; r and α are the polar radius and polar angle in the polar coordinate system (r - α), respectively; P and λ are the power loss density and thermal conductivity of the corresponding heat zone, respectively.

Thus, for active zones, when they exhibit a periodic annular distribution, the general solution of the temperature distribution function T can be expressed as:

$$T = \vartheta_1 + \vartheta_2 \ln(r) + \Theta P + \sum_n \left[\vartheta_{3n} \left(\frac{r}{R_o} \right)^n + \vartheta_{4n} \left(\frac{r}{R_i} \right)^{-n} \right] \cos(n\alpha) + \sum_n \left[\vartheta_{5n} \left(\frac{r}{R_o} \right)^n + \vartheta_{6n} \left(\frac{r}{R_i} \right)^{-n} \right] \sin(n\alpha) \quad (9)$$

And when they exhibit a periodic sector distribution, the general solution T can be expressed as:

$$T = \vartheta_1 + \vartheta_2 \ln(r) + \Theta P + \sum_u \left[\vartheta_{3u} \left(\frac{r}{R_o} \right)^{E_u} + \vartheta_{4u} \left(\frac{r}{R_i} \right)^{-E_u} \right] \cos \left[E_u \left(\alpha - \theta + \frac{\tau}{2} \right) \right] + \sum_t \left[\vartheta_{5t} f_{5t} + \vartheta_{6t} f_{6t} \right] \sin \left[E_t \ln \left(\frac{r}{R_i} \right) \right] \quad (10)$$

where

$$f_{5t} = \frac{\sinh \left[E_t \left(\alpha - \theta + \frac{\tau}{2} \right) \right]}{\sinh(\tau E_t)}, \quad f_{6t} = \frac{\sinh \left[E_t \left(\alpha - \theta - \frac{\tau}{2} \right) \right]}{\sinh(\tau E_t)} \quad (11)$$

where $\vartheta_1, \vartheta_2, \vartheta_{3n}, \vartheta_{4n}, \vartheta_{5n}, \vartheta_{6n}, \vartheta_{3u}, \vartheta_{4u}, \vartheta_{5t}$, and ϑ_{6t} are the coefficients to be solved; R_o, R_i, θ , and τ are the outer radius, inner radius, center position angle, and spanning angle of the corresponding zone, respectively; ΘP is the special solution term, $\Theta P = -Pr^2/(4\lambda)$; $E_u = u\pi/\tau$; $E_t = t\pi/\ln(R_o/R_i)$; $n = 1, 2, 3, \dots$; $u = 1, 2, 3, \dots$; $t = 1, 2, 3, \dots$.

In a similar way, the general solution of the temperature distribution function T for other passive zones in the x - y plane can be derived. Compared to active zones, only the special solution term ΘP is omitted.

2) z -axis Direction

When the rotation angle is changed, the cross-sections along the z -axis direction are different. This conclusion is discussed in detail in the previous part. Here, the general solution for the temperature of each heat zone on the most interesting and most complex equivalent cross-section 1 is derived. For all other equivalent cross-sections, reference is made to the treatment of equivalent cross-section 1.

Likewise, based on the actual heat generation during operation, the equivalent heat zones can be divided into two categories: active zones (HZ-B, HZ-C, HZ-E, HZ-F, and HZ-H) and passive zones (HZ-A, HZ-D, HZ-G, HZ-I, HZ-J, HZ-K, and HZ-L). Then, the corresponding heat partial differential equation in the z -axis direction can be expressed as:

$$\frac{\partial^2 T}{\partial r^2} + \frac{1}{r} \frac{\partial T}{\partial r} + \frac{1}{r^2} \frac{\partial^2 T}{\partial z^2} = \begin{cases} -P/\lambda & \text{Active zones} \\ 0 & \text{Passive zones} \end{cases} \quad (12)$$

where z is the vertical coordinate in the Cartesian coordinate system (r - z).

Thus, for active zones, when they exhibit an axial penetrating distribution, the general solution of the temperature distribution function T can be expressed as:

$$T = \gamma_1 + \gamma_2 \ln(r) + \Theta P + \sum_k \left[\gamma_{3k} \left(\frac{r}{R_o} \right)^k + \gamma_{4k} \left(\frac{r}{R_i} \right)^{-k} \right] \cos \left(\frac{2\pi k z}{L_{\text{housing}}} \right) + \sum_k \left[\gamma_{5k} \left(\frac{r}{R_o} \right)^k + \gamma_{6k} \left(\frac{r}{R_i} \right)^{-k} \right] \sin \left(\frac{2\pi k z}{L_{\text{housing}}} \right) \quad (13)$$

And when they exhibit an axial non-penetrating distribution, the general solution T can be expressed as:

$$T = \gamma_1 + \gamma_2 \ln(r) + \Theta P + \sum_v \left[\gamma_{3v} \left(\frac{r}{R_o} \right)^{E_v} + \gamma_{4v} \left(\frac{r}{R_i} \right)^{-E_v} \right] \cos \left[E_v \left(z - \zeta + \frac{\kappa}{2} \right) \right] + \sum_h \left[\gamma_{5h} g_{5h} + \gamma_{6h} g_{6h} \right] \sin \left[E_h \ln \left(\frac{r}{R_i} \right) \right] \quad (14)$$

where

$$g_{5h} = \frac{\sinh \left[E_h \left(z - \zeta + \frac{\kappa}{2} \right) \right]}{\sinh(\kappa E_h)}, \quad g_{6h} = \frac{\sinh \left[E_h \left(z - \zeta - \frac{\kappa}{2} \right) \right]}{\sinh(\kappa E_h)} \quad (15)$$

where $\gamma_1, \gamma_2, \gamma_{3k}, \gamma_{4k}, \gamma_{5k}, \gamma_{6k}, \gamma_{3v}, \gamma_{4v}, \gamma_{5h}$, and γ_{6h} are the coefficients to be solved; L_{housing} is the housing axial length; ζ is the angle mapped by the vertical coordinate of the center position of the corresponding zone; κ is the spanning angle mapped by the axial length L_{HZ} of the corresponding zone, and $\kappa = 2\pi L_{\text{HZ}}/L_{\text{housing}}$; $E_v = v\pi/\kappa$; $E_h = h\pi/\ln(R_o/R_i)$; $k = 1, 2, 3, \dots$; $v = 1, 2, 3, \dots$; $h = 1, 2, 3, \dots$.

In a similar way, the general solution of the temperature distribution function T for other passive zones in the z -axis direction can be derived. Compared to active zones, only the special solution term ΘP is omitted.

C. Solving of 3D TAM

First, appropriate boundary conditions are established based on the intersection features between neighboring heat zones.

As depicted in Fig. 11, the boundaries can be divided into two categories: internal boundaries (black solid lines) and external boundaries (red solid lines). The internal boundaries are formed by the interfaces between neighboring heat zones. Assuming that the contact between neighboring heat zones is ideal, and then combining it with the heat flux continuity theorem, the boundary conditions on all internal boundaries can be obtained. Fig. 12 depicts the internal boundaries of one representative region, where r_1, r_2 , and r_3 are the boundary radius; α_1, α_2 and α_3 are the boundary angle. When the radius is equal to r_2 , the boundary conditions between HZ-3 and HZ-1 & HZ-2 can be expressed as:

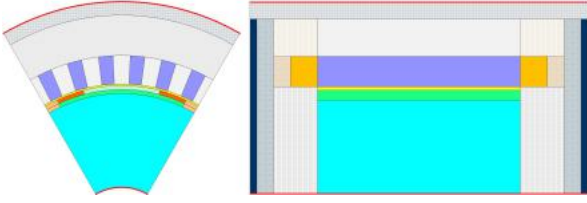


Fig. 11. Classification of boundary conditions.

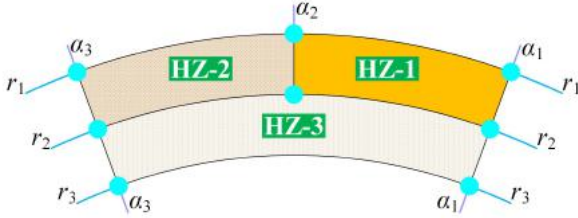


Fig. 12. Internal boundaries of one representative region.

$$T_3 = T_1 \quad \text{for } \alpha \in [\alpha_1, \alpha_2] \quad (16)$$

$$T_3 = T_2 \quad \text{for } \alpha \in [\alpha_2, \alpha_3] \quad (17)$$

$$\chi_{3r} = \begin{cases} \chi_{1r} & \text{for } \alpha \in [\alpha_1, \alpha_2] \\ \chi_{2r} & \text{for } \alpha \in [\alpha_2, \alpha_3] \end{cases} \quad (18)$$

where T_1 , T_2 , and T_3 are the temperature distribution functions of HZ-1, HZ-2, and HZ-3, respectively; χ_{1r} , χ_{2r} , and χ_{3r} are the radial heat flux density functions of HZ-1, HZ-2, and HZ-3, respectively. When the angle is equal to α_2 , the boundary conditions between HZ-1 and HZ-2 can be expressed as:

$$T_1 = T_2 \quad \text{for } r \in [r_1, r_2] \quad (19)$$

$$\chi_{1\alpha} = \chi_{2\alpha} \quad \text{for } r \in [r_1, r_2] \quad (20)$$

where $\chi_{1\alpha}$ and $\chi_{2\alpha}$ are the tangential heat flux density functions of HZ-1 and HZ-2 respectively. The external boundaries, on the other hand, are formed by the interface between the housing and the ambient as well as the interface between the rotor and the shaft. For the former, the boundary condition on it can be obtained directly with reference to the ambient temperature. That is, it can be expressed as:

$$\chi_{hr} |_{r=R_{\text{ext}}} = \lambda_{\text{ext}} (T_h |_{r=R_{\text{ext}}} - T_{\text{ambient}}) \quad (21)$$

where T_h and χ_{hr} are the temperature and radial heat flux density of the housing, respectively; R_{ext} is the outer radius of the housing; λ_{ext} is the heat dissipation coefficient of the ambient; T_{ambient} is the ambient temperature. Similarly, for the latter, the boundary condition on it can be obtained with reference to the shaft temperature. That is, it can be expressed as:

$$\chi_{rr} |_{r=R_{\text{int}}} = -\lambda_{\text{int}} (T_r |_{r=R_{\text{int}}} - T_{\text{shaft}}) \quad (22)$$

where T_r and χ_{rr} are the temperature and radial heat flux density of the rotor, respectively; R_{int} is the inner radius of the rotor; λ_{int} is the heat dissipation coefficient of the shaft; T_{shaft} is the shaft temperature.

It can be seen that to complete the establishment of the above boundary conditions, it is also necessary to know the specific values of T_{ambient} and T_{shaft} . For T_{ambient} , this can be obtained by reasonable assumptions or by direct measurement

from the actual operating environment. And for T_{shaft} , both means are clearly inappropriate and unpersuasive. For this purpose, a simplified LPTNM is introduced as depicted in Fig. 13. 1) With reference to the geometric features of each component, their T-type thermal models are built. 2) The built T-type thermal models are connected according to the actual heat transfer paths to form the simplified LPTNM. 3) The specific value of T_{shaft} is then obtained.

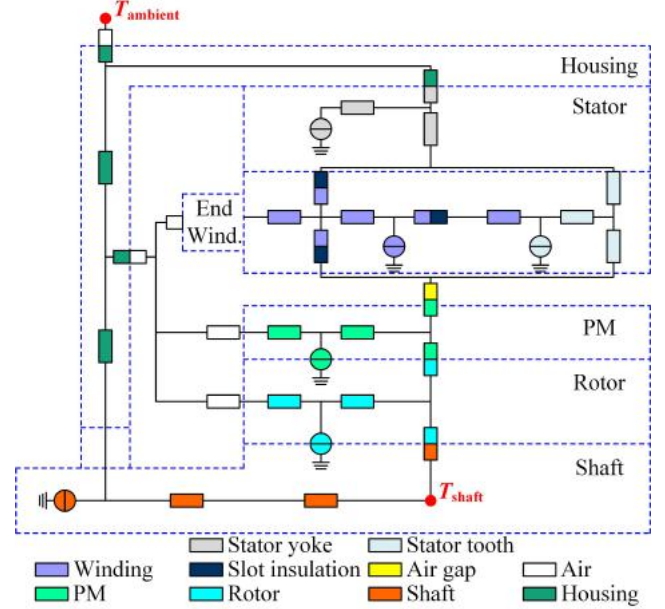


Fig. 13. Simplified LPTNM.

Next, the system of equations consisting of the boundary conditions can be constructed. This can be expressed as:

$$C_{\text{coe}} \cdot [\boldsymbol{\vartheta}, \boldsymbol{\gamma}]^T = \boldsymbol{Y} \quad (23)$$

where C_{coe} is the coefficient matrix; $[\boldsymbol{\vartheta}, \boldsymbol{\gamma}]^T$ is the transpose matrix of the matrix formed by the coefficients to be solved; \boldsymbol{Y} is the constant term matrix.

Then, the specific values of all the coefficients to be solved are obtained by solving (23). The analytical solution of the temperature distribution function for each heat zone is also obtained. Further, if the errors in the average temperatures of critical components calculated by LPTNM and TAM are large, it is necessary to update the relevant settings, including but not limited to equivalent convective heat dissipation coefficients and material properties. Eventually, the boundary conditions are adjusted and the above process is repeated until the error meets the need to complete the solving of TAM. This in turn realizes the fast calculation of key thermal characteristics.

V. ELECTROMAGNETIC THERMAL COUPLING ANALYTICAL MODEL

In order to fully account for the strong coupling between the electromagnetic field and the temperature field of motors, a novel ETcAM is proposed on the basis of the aforementioned studies, as depicted in Fig. 14. The specific implementation process can be summarized as follows.

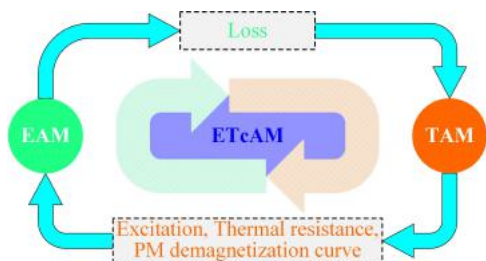


Fig. 14. Proposed ETcAM.

1) Build the information transmission channel between EAM and TAM by referring to the intrinsic connection between the electromagnetic field and the temperature field.

2) Realize the fast calculation of key electromagnetic characteristics by EAM.

3) Mapping the loss calculated by EAM to TAM. Realize the fast calculation of key thermal characteristics.

4) Based on the temperature calculated by TAM, rationally adjust the PM demagnetization curve, thermal resistance, excitation source, and so on.

5) Perform steps 2), 3), and 4) again to compare the results of the previous and subsequent calculations. Until the results of the two calculations are stabilized. Then the solving of ETcAM is completed.

6) Eventually, the fast and accurate prediction of the electromagnetic and temperature fields for the SPMSM equipped with unequally thick magnetic poles is realized.

The proposed ETcAM not only inherits the rapidity of EAM and TAM in the calculation of electromagnetic and thermal characteristics, but also most realistically reproduces the actual operating situation, which further improves the calculation accuracy. In addition, the proposed ETcAM saves a lot of computer resources. It provides unlimited possibilities for the initial design, scheme evaluation, and optimization of motors.

VI. COMPARISON AND VALIDATION

In this section, a comparative analysis and experimental validation of a 11 kW SPMSM equipped with unequally thick magnetic poles is carried out to validate this study. The main configuration of this SPMSM is shown in Table II.

TABLE II
KEY CONFIGURATIONS AND HEAT DISSIPATION CONDITIONS

Parameters	Value
Stator outer/Inner radius/mm	130/90
Rotor outer/Inner radius/mm	89/30
Effective axis length/mm	79
Number of poles/slots	6/36
Rated speed/(r/min)	1500
Rated power/kW	11
Cooling form	Natural air-cooling
Insulation grade	H

A. Computational Fluid Dynamics

Along with the development of computer technology and numerical technology, CFD has gradually become a powerful tool for engineers and researchers to address and analyze

engineering thermal problems. There is no doubt that CFD can do an extremely good job of predicting the temperature field of various types of motors. For this reason, in addition to FEM, CFD (3D) is also introduced to validate this study. In addition, there are several settings that need to be specifically declared when applying CFD: 1) The gravity is not considered. 2) The internal fluid is considered incompressible. 3) The polyhedral mesh with high mesh quality is adopted, as depicted in Fig. 15.

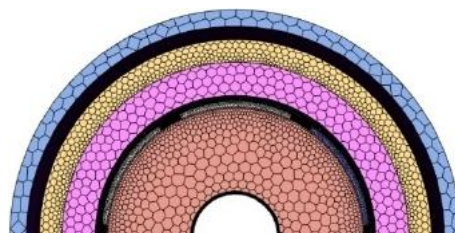


Fig. 15. CFD mesh.

B. Experimental Platform

Fig. 16 shows the experimental test site. In the built high-performance experimental platform: 1, prime mover; 2, torque transducer; 3, tested prototype; 4, infrared thermal imager; 5, oscilloscope; 6, converter; 7, notebook; 8, power analyzer; 9, multi-channel paperless temp recorder. It can be observed that circular temperature measurement holes have been drilled in the end cap in alignment with the PM in order to facilitate the measurement of the temperature on the mover side. Through these holes, the temperature of the PM and the rotor can be measured using an infrared thermal imager. And for the temperature on the stationary side, it can be easily measured using pre-embedded sensors. In short, the measurement of electromagnetic characteristics and thermal characteristics can be accomplished excellently with this platform.

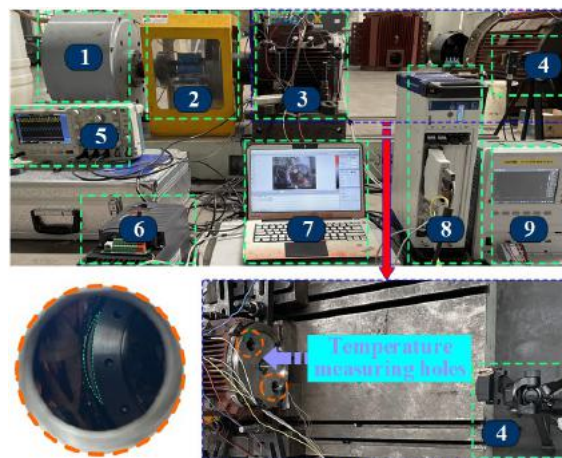


Fig. 16. Test site.

C. Comparison of ETcAM, Simulation, and Experiment

1) Comparison of the Electromagnetic Field

Fig. 17 illustrates the key electromagnetic characteristics obtained by ETcAM, FEM, and experiment: the no-load phase electromotive force and the on-load electromagnetic torque. It is easy to observe that the waveform distributions of these two characteristics obtained by the three methods have a very high

coincidence. Through comparison, the valid values of no-load phase electromotive force obtained from ETcAM, FEM, and experiment are 204.22 V, 198.56 V, and 198.70 V, respectively; the fundamental amplitudes of no-load phase electromotive force are 288.79 V, 280.76 V, and 280.94 V, respectively; the average values of on-load electromagnetic torque are 69.69 N·m, 69.38 N·m, 69.39 N·m; the peak to peak values of on-load electromagnetic torque are 0.51 N·m, 1.06 N·m, 1.49 N·m. The differences among them are very small. Such a small difference is very acceptable considering that mesh profiling, magnetic leakage, processes, measurements, etc. can contribute to these differences. Therefore, the outstanding prediction capability of ETcAM for the electromagnetic field is well demonstrated.

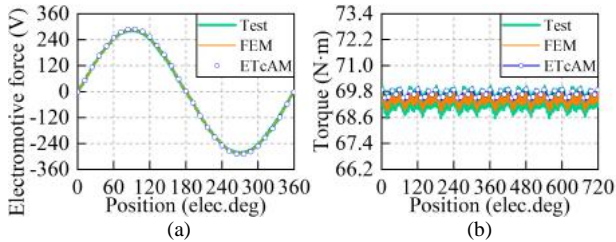


Fig. 17. Comparison of electromagnetic characteristics. (a) Electromotive force. (b) Torque.

2) Comparison of the Temperature Field

A careful comparison of the key thermal characteristics calculated by ETcAM and CFD is presented. First, the two most representative cross-sections in 3D space along the x - y plane and the z -axis direction, respectively, are selected to be used as comparison cross-sections, as depicted in Fig. 18. Fig. 19 and Fig. 20 illustrate the temperature distributions in the x - y plane and in the z -axis direction calculated by ETcAM and CFD, respectively. It can be noticed that the temperature distributions calculated by both methods have a very high degree of similarity. The regions with the most severe heating are both found on the in-slot winding and the end winding, respectively. It is also important to explain that there is a slight difference between the temperature distributions calculated by the two methods in the transition region from the in-slot winding to the stator yoke. The main reason for this phenomenon is that the CFD fully accounts for the complex structure of the slot including the insulation and double-layer winding, and does not use an equivalent topology that matches with ETcAM. Only this validation is convincing enough. However, the good news is that ETcAM is properly equivalent to the in-slot winding, which makes it still perform well. Next, the temperature variations along the path of greatest interest (i.e., the path aligned with the pole centerline and slot centerline) calculated by ETcAM and CFD are compared, as illustrated in Fig. 21. It can be noticed that still, except for a slight difference in the transition region, the temperature variations calculated by both methods are almost identical. On this path, the calculated average deviations between the two methods regarding the rotor, PM, winding, stator, and housing are only 0.17%, 0.09%, 3.35%, 3.27%, and 2.53%, respectively. Further, the maximum temperatures calculated by ETcAM and CFD are compared, as illustrated in

Fig. 22. It can be noticed that the maximum temperatures of the individual components calculated by both methods are almost the same. The maximum temperatures of the rotor, PM, winding, stator, and housing calculated by ETcAM are 97.83 °C, 99.82 °C, 113.49 °C, 97.48 °C, and 82.81 °C, respectively, while those calculated by CFD are 101.17°C, 101.10 °C, 117.33 °C, 100.80 °C, and 83.06 °C, respectively. The deviations between the two methods are very small and impressive, being only 3.30%, 1.27%, 3.27%, 3.29%, and 0.30% with respect to the rotor, PM, winding, stator, and housing, respectively. Finally, the measured temperatures are illustrated in Fig. 23. The error between the ETcAM as well as CFD calculations and the measured data is very small. Again, such a small error is very acceptable considering the effects of many factors such as machining, assembly, and measurement. Therefore, the outstanding prediction capability of ETcAM for the temperature field is well demonstrated.

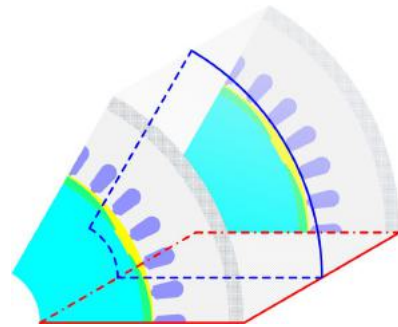


Fig. 18. Comparison cross sections in the x - y plane (blue outline) and z -axis direction (red outline).

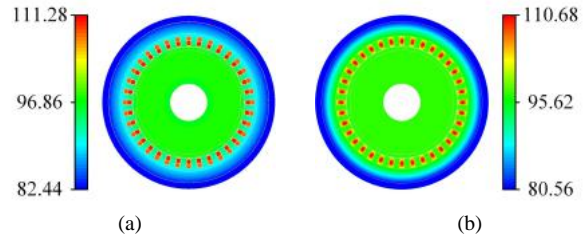


Fig. 19. Temperature distribution in the x - y plane. (a) CFD, unit: °C. (b) ETcAM, unit: °C.

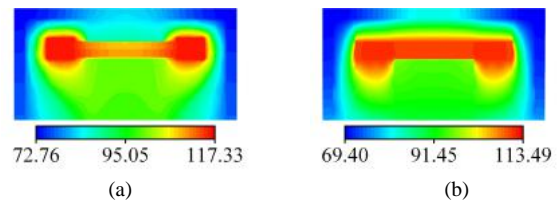


Fig. 20. Temperature distribution in the z -axis direction. (a) CFD, unit: °C. (b) ETcAM, unit: °C.

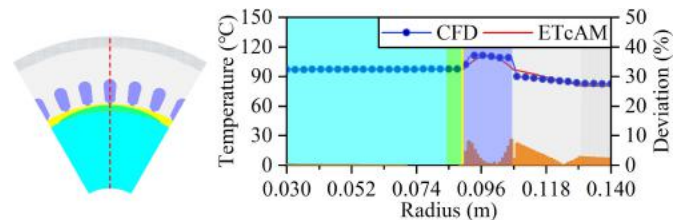


Fig. 21. Temperature variation along the path aligned with the pole centerline and slot centerline.

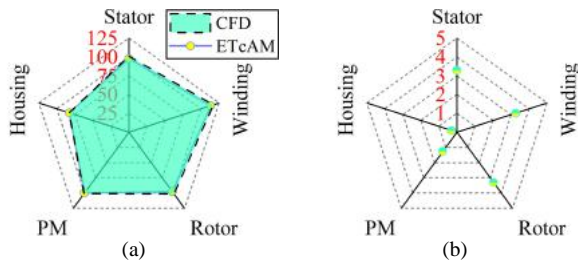


Fig. 22. Maximum temperature of critical components. (a) Maximum value, unit: °C. (b) Deviation, unit: %.

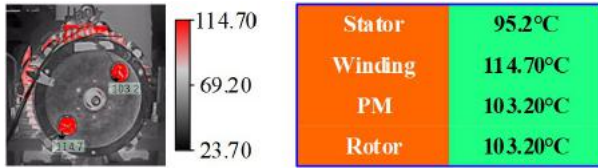


Fig. 23. Measured temperature.

3) Comparison of computational costs

Table III lists the computational costs of the different methods for the same computer configuration. Compared to FEM, the studied EAM is able to save nearly 81.00% of time and 99.95% of storage by performing a single electromagnetic field calculation. Compared to CFD, the developed TAM is able to save nearly 78.72% of time and 94.54% of storage by performing a single temperature field calculation. It is due to the excellent performance of EAM and TAM in terms of computational cost consumption that the proposed ETcAM has been accomplished, making it possible to save nearly 99.12% of the time and 93.57% of the storage to perform a complete electromagnetic thermal analysis.

TABLE III
COMPUTATIONAL COSTS OF DIFFERENT METHODS

Item		Time/min	Storage/MB
Elec. field	FEM	6.42	361.07
	EAM	1.22	0.19
	Difference/(%)	81.00	99.95
Temp. field	CFD	53.38	1301.02
	TAM	11.36	71.09
	Difference/(%)	78.72	94.54
Elec. & Temp.	FEM & CFD	239.20	6648.36
	ETcAM	2.10	427.68
	Difference/(%)	99.12	93.57

Therefore, the outstanding advantages of the proposed ETcAM in terms of computational cost consumption are quite recognizable.

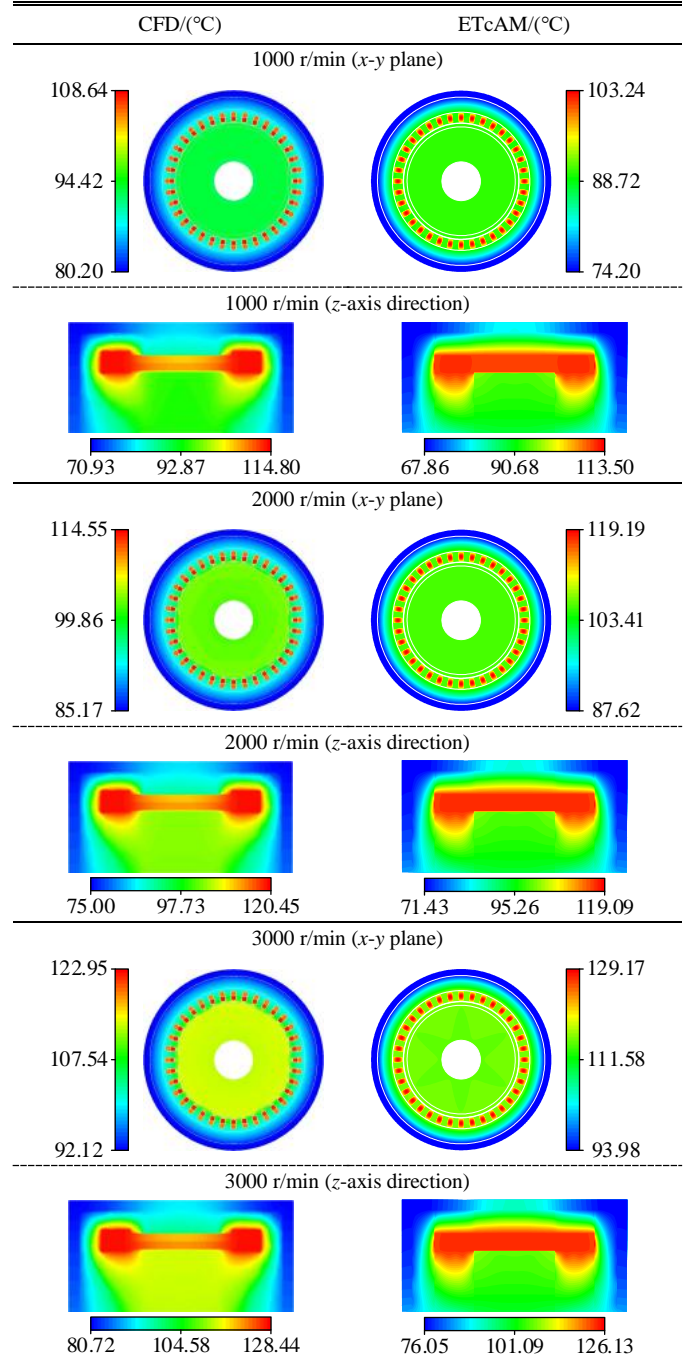
D. Discussion of Model Robustness

In the actual operation of the motor, need to face a variety of complex operating conditions. Therefore, it is necessary to discuss the performance of the proposed ETcAM when the operating conditions change in order to further verify the model robustness.

Table IV lists the global temperature distributions calculated by the different methods when the speed is varied at rated load. Three specific speeds are compared: 1000 r/min, 2000 r/min, and 3000 r/min. It is easy to find that the global

temperature distributions of the proposed ETcAM and CFD are basically the same no matter what kind of variable speed operating conditions. Regarding the heat generation area, hot spot location, and change trend at 1000 r/min, 2000 r/min, and 3000 r/min respectively, the calculation results of the proposed ETcAM and CFD are very much in line with each other. The computational differences between the two methods are very small. The model robustness of the proposed ETcAM is further confirmed by the above discussion. In conclusion, the proposed ETcAM can flexibly respond to the changes in the operating conditions of the motor and realize the fast and accurate calculation of key thermal characteristics.

TABLE IV
TEMPERATURE DISTRIBUTION UNDER DIFFERENT OPERATING CONDITIONS



VII. CONCLUSION

In this article, the SPMSM equipped with unequally thick magnetic poles is taken as the main research object, and its ETcAM is investigated in a series.

First, the EAM used to calculate the key electromagnetic characteristics is studied. Subsequently, the TAM used to calculate the key thermal characteristics in 3D space is developed. Further, the novel ETcAM is proposed. The fast and accurate prediction of electromagnetic and temperature fields is realized. The ETcAM well accounts for the complex structure, saturation, and heat exchange behavior. In addition, it saves a large amount of computer resources and provides unlimited possibilities for the initial design, scheme evaluation, and optimization of motors.

In particular, it is also important to state that this study faces certain limitations despite its usefulness in realizing the electromagnetic thermal analysis of motors and boosting the efficient and intelligent design of motors. Specifically, when modeling the EAM for the electromagnetic field analysis, end effects are not considered for the convenience of subdomain subdivision, general solution derivation, boundary condition establishment, and model solving. This partial simplification leads to the inability to accurately capture the heat source changes caused by end leakage and axial eddy currents, which may have some negative impact on the model solution accuracy. Therefore, in the subsequent study, the focus will be on the improvement of EAM and the innovative combination with other methods (e.g., magnetic equivalent circuit and other methods) to analyze the end effects more accurately and to improve the model solution accuracy in a comprehensive way.

REFERENCES

- [1] K. T. Chau, C. C. Chan, and C. H. Liu, "Overview of Permanent-magnet Brushless Drives for Electric and Hybrid Electric Vehicles," *IEEE Trans. on Ind. Electron.*, vol. 55, no. 6, pp. 2246–2257, Jun. 2008.
- [2] C. Y. He, and T. Wu, "Analysis and Design of Surface Permanent Magnet Synchronous Motor and Generator," *CES Trans. on Electr. Mach. and Syst.*, vol. 3, no. 1, pp. 94–100, Mar. 2019.
- [3] J. K. Si, S. Z. Zhao, and H. C. Feng *et al.*, "Analysis of Temperature Field for a Surface-mounted and Interior Permanent Magnet Synchronous Motor Adopting Magnetic-thermal Coupling Method," *CES Trans. on Electr. Mach. and Syst.*, vol. 2, no. 1, pp. 166–174, Mar. 2018.
- [4] C. T. Chen, X. Z. Wu, and X. B. Yuan *et al.*, "A New Technique for the Subdomain Method in Predicting Electromagnetic Performance of Surface-mounted Permanent Magnet Motors with Shaped Magnets and a Quasi-regular Polygon Rotor Core," *IEEE Trans. on Energy Convers.*, vol. 38, no. 2, pp. 1396–1409, Jun. 2023.
- [5] Z. Q. Zhu, W. Q. Chu, and Y. Guan, "Quantitative Comparison of Electromagnetic Performance of Electrical Machines for HEVs/EVs," *CES Trans. on Electr. Mach. and Syst.*, vol. 1, no. 1, pp. 37–47, Mar. 2017.
- [6] L. Balasubramanian, N. A. Bhuiyan, and A. Javied *et al.*, "Design and Optimization of Interior Permanent Magnet (IPM) Motor for Electric Vehicle Applications," *CES Trans. on Electr. Mach. and Syst.*, vol. 7, no. 2, pp. 202–209, Jun. 2023.
- [7] X. D. Liu, H. Chen, and J. Zhao *et al.*, "Research on the Performances and Parameters of Interior PMSM Used for Electric Vehicles," *IEEE Trans. on Ind. Electron.*, vol. 63, no. 6, pp. 3533–3545, Jun. 2016.
- [8] M. Q. Wang, P. Zheng, and C. D. Tong *et al.*, "Research on a Transverse-flux Brushless Double-rotor Machine for Hybrid Electric Vehicles," *IEEE Trans. on Ind. Electron.*, vol. 66, no. 2, pp. 1032–1043, Feb. 2019.
- [9] L. J. Wu, H. Yin, and D. Wang *et al.*, "On-load Field Prediction in SPM Machines by a Subdomain and Magnetic Circuit Hybrid Model," *IEEE Trans. on Ind. Electron.*, vol. 67, no. 9, pp. 7190–7201, Sept. 2020.
- [10] W. F. Yu, K. Liu, and W. Hua *et al.*, "A New High-speed Dual-stator Flux Switching Permanent Magnet Machine with Distributed Winding," *IEEE Trans. on Magn.*, vol. 58, no. 2, pp. 1–6, Feb. 2022.
- [11] G. H. Liu, Y. Wang, and Q. Chen *et al.*, "Design and Analysis of a New Equivalent Magnetic Network Model for IPM Machines," *IEEE Trans. on Magn.*, vol. 56, no. 6, pp. 1–12, Jun. 2020.
- [12] C. T. Chen, X. Z. Wu, and X. B. Yuan *et al.*, "Hybrid Analytical Model for Air-gap Magnetic Field Prediction of Surface-mounted Permanent Magnet Motors with a Quasi-regular Polygon Rotor," *IET Electr. Power Appl.*, vol. 17, no. 9, pp. 1136–1147, Sept. 2023.
- [13] F. Liu, X. H. Wang, and H. Y. Wei, "Improved Multiphysics Multiobjective Optimization for U-shaped IPMSM Equipped with Eccentric Rotor," *IEEE J. of Emerging and Sel. Top. in Power Electron.*, vol. 11, no. 5, pp. 5131–5144, Oct. 2023.
- [14] W. M. Tong, S. N. Wu, and R. Y. Tang, "Totally Enclosed Self-circulation Axial Ventilation System Design and Thermal Analysis of a 1.65-MW Direct-drive PMSM," *IEEE Trans. on Ind. Electron.*, vol. 65, no. 12, pp. 9388–9398, Dec. 2018.
- [15] K. Boughrara, F. Dubas, and R. Ibtouen, "2-D Exact Analytical Method for Steady-state Heat Transfer Prediction in Rotating Electrical Machines," *IEEE Trans. on Magn.*, vol. 54, no. 9, pp. 1–19, Sept. 2018.
- [16] F. Liu, and X. H. Wang, "Design and Multiobjective Optimization of Dual-circulation Cooling System Considering Electro-thermal Coupling for IPMSM," *IEEE Trans. on Transp. Electrification*, vol. 9, no. 2, pp. 3072–3084, Jun. 2023.
- [17] A. Boglietti, A. Cavagnino, and D. Staton *et al.*, "Evolution and Modern Approaches for Thermal Analysis of Electrical Machines," *IEEE Trans. on Ind. Electron.*, vol. 56, no. 3, pp. 871–882, Mar. 2009.
- [18] A. J. Grobler, S. R. Holm, and G. van Schoor, "A Two-dimensional Analytic Thermal Model for a High-speed PMSM Magnet," *IEEE Trans. on Ind. Electron.*, vol. 62, no. 11, pp. 6756–6764, Nov. 2015.
- [19] D. W. Liang, Z. Q. Zhu, and B. Shao *et al.*, "Tracking of Winding and Magnet Hotspots in SPMSMs based on Synergized Lumped-parameter and Sub-domain Thermal Models," *IEEE Trans. on Energy Convers.*, vol. 37, no. 3, pp. 2147–2161, Sept. 2022.
- [20] X. Li, X. H. Wang, and Z. Z. Xing, "Analysis and Research on Local Irreversible Demagnetization of Inverter-powered PM Motor," *IEEE Trans. on Ind. Electron.*, vol. 71, no. 6, pp. 5618–5629, Jun. 2024.
- [21] C. López-Torres, A. Garcia, and J. R. Riba *et al.*, "Computationally Efficient Design and Optimization Approach of PMA-synRM in Frequent Operating Torque-speed Range," *IEEE Trans. on Energy Convers.*, vol. 33, no. 4, pp. 1776–1786, Dec. 2018.
- [22] J. Ren, X. H. Wang, and W. L. Zhao *et al.*, "Torsional Vibration Analysis and Optimization Design of the Surface PM Synchronous Machine with Reduced Torque Ripple," *IEEE Trans. on Transp. Electrification*, vol. 10, no. 3, pp. 5842–5852, Sept. 2024.



Feng Liu was born in China on November 1997. He received the B.E. degree in electrical engineering from Qingdao University, Qingdao, China, in 2020. He is currently working toward the Ph.D. degree in the School of Electrical Engineering, Shandong University, Jinan, China.

His current research interests include design and analysis of permanent magnet machines, motor drive and control on electric vehicle.



Xiuhe Wang was born in China on July 1967. He received the B.E. and M.E. degrees in electrical engineering from Shandong University, Jinan, China, in 1989 and 1993, respectively, and the Ph.D. degree in electrical engineering from Shenyang University of Technology, Shenyang, China, in 1996.

From 2001 to 2002, he was a Postdoctoral Fellow with Seoul National University, Seoul, South Korea. He currently holds the positions of a Professor of Electrical Engineering and the Vice Head for the School of Electrical Engineering, Shandong University. His research interests include permanent magnet machines, theoretical analysis and calculation of electromagnetic devices, and artificial intelligence and its application on electrical machines. He has authored/coauthored more than 200 papers on these topics.



Lingling Sun was born in China, in December 1967. She received the B.E., M.E., and Ph.D. degrees from Shandong University, Jinan, China, in 1990, 1993, and 2004, respectively. She is currently a Professor of mechanical engineering and the Vice Director of the School of Mechanical Engineering, Shandong

University.

Her research interests include vibration theory and application, vibration and noise of mechanical equipment, vehicle system dynamics.



Hongye Wei was born in China on July 1998. She received the B.E. degree in energy and power engineering from Central South University of Forestry and Technology, Changsha, China, in 2020. She is currently working toward the M.E. degree in the School of Electrical Engineering, Shandong University, Jinan,

China.

Her current research interests include design, analysis and optimization of permanent magnet machines and synchronous reluctance motors.